Viscoelastic fluid-structure interactions between a flexible cylinder and wormlike micelle solution

Anita A. Dey, Yahya Modarres-Sadeghi, and Jonathan P. Rothstein*
Department of Mechanical and Industrial Engineering, University of Massachusetts Amherst, Amherst, Massachusetts 01003, USA

(Received 20 December 2017; published 11 June 2018)

It is well known that when a flexible or flexibly mounted structure is placed perpendicular to the flow of a Newtonian fluid, it can oscillate due to the shedding of separated vortices at high Reynolds numbers. Unlike Newtonian fluids, the flow of viscoelastic fluids can become unstable even at infinitesimal Reynolds numbers due to a purely elastic flow instability that can occur at large Weissenberg numbers. Recent work has shown that these elastic flow instabilities can drive the motion of flexible sheets. The fluctuating fluid forces exerted on the structure from the elastic flow instabilities can lead to a coupling between an oscillatory structural motion and the state of stress in the fluid flow. In this paper, we present the results of an investigation into the flow of a viscoelastic wormlike micelle solution past a flexible circular cylinder. The time variation of the flow field and the state of stress in the fluid are shown using a combination of particle image tracking and flow-induced birefringence images. The static and dynamic responses of the flexible cylinder are presented for a range of flow velocities. The nonlinear dynamics of the structural motion is studied to better understand an observed transition from a symmetric to an asymmetric structural deformation and oscillation behavior.

DOI: 10.1103/PhysRevFluids.3.063301

I. INTRODUCTION

A. Non-Newtonian fluid instabilities

Non-Newtonian fluids such as viscoelastic fluids exhibit many interesting characteristics, the most important being that they may behave like an elastic Hookean solid or a viscous Newtonian fluid or a complex combination of the two, depending on the timescale in which they are investigated. The combination of viscosity and elasticity is imparted by the physical nature of the macromolecules in these fluids, which may be present in the form of high-molecular-weight polymers, self-assembled wormlike micelles, or suspensions of micron or nanoscale particles. As a flexible polymer coil or wormlike micelle stretches within a flow field, it is deformed out of its equilibrium random configuration. An elastic restoring force results, driving the polymer or micelle back toward its entropically favorable equilibrium state [1]. This leads to a characteristic fluid timescale known as the relaxation time $\lambda = \eta/G$, which describes the time required for the polymer coil or wormlike micelle to relax from a deformed state back to its equilibrium configuration [2]. Here η is the viscosity and G is the elastic modulus of the fluid. For these fluids, Newton's law of viscosity no longer holds. They are therefore described as non-Newtonian fluids. For these fluids, it takes a finite time for elastic stress built up by the flow to grow or decay, thus the residence time of a fluid in a flow must also be considered to understand the viscoelastic fluid's response. The relative importance of elasticity in a flow is described by a Deborah number, which is the ratio of the relaxation time of the

*rothstein@ecs.umass.edu

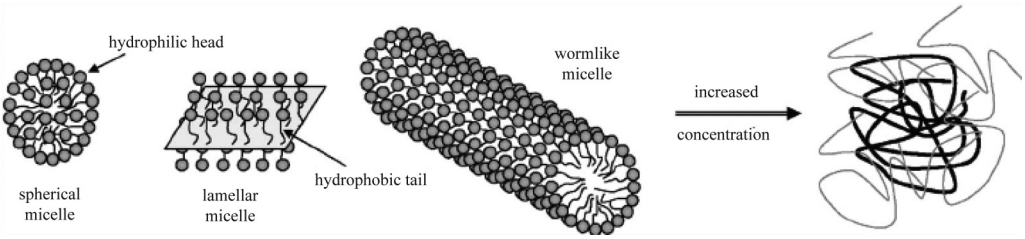

FIG. 1. Various morphologies of wormlike micelles which impart viscoelasticity [12].

fluid to a characteristic deformation timescale $\mathrm{De} = \lambda / t_{\mathrm{flow}}$. If the deformation timescale is large in comparison to the relaxation time of the fluid $\mathrm{De} \ll 1$, then the polymer coil or wormlike micelle has ample time to relax back to equilibrium and the fluid will behave like a Newtonian fluid. If the relaxation time is much longer than the deformation timescale in the flow $\mathrm{De} \gg 1$, then the fluid will react like an elastic Hookean solid [2]. The behavior of the fluid between these two extremes is quite rich and that is where this study will concentrate.

Viscoelastic wormlike micelle solutions are used extensively as rheological modifiers in consumer products such as paints, detergents, pharmaceuticals, lubricants, and emulsifiers where careful control of the fluid properties is required. In addition, micelle solutions have become important in a wide range of applications including agrochemical spraying, inkjet printing, turbulent drag reduction, and enhanced oil recovery where they are often used as a polymer-free fracture fluid for stimulating oil production [3–5]. A fundamental understanding of the behavior of these complex fluids in different flow regimes is therefore extremely important to a host of industries. Techniques for the analysis and control of the flow of complex fluids require accurate determination of material properties as well as the ability to understand and predict changes that occur within the materials as they are subjected to the flow conditions encountered in industrial and commercial applications. Shear and extensional rheometers provide an excellent framework for investigating the behavior of these complex fluids, because the flow kinematics tends to be simple. Additionally, these rheological measurements can shed light on the dynamics of wormlike micelle solutions in complex flows and phenomena such as elastic flow instabilities, which commonly occur in many of the industrial and commercial applications. A number of studies of the nonlinear rheology and the behavior of these complex fluids in strong flows have recently been published [6–8].

Wormlike micelle solutions are comprised of amphiphilic surfactant molecules which have both a bulky hydrophilic head, which is often charged, and a relatively short and slender hydrophobic tail, typically consisting of an 8–20 carbon atom chain. Above their critical micelle concentration (CMC), surfactant molecules in water will spontaneously self-assemble into large aggregates known as micelles to minimize the exposure of their tails to water [9–11]. As can be seen in Fig. 1, these large aggregates can form into a number of different complex shapes including spherical and wormlike micelles, vesicles, and lipid bilayers [13]. The morphology of the aggregates depends on the size of the surfactant head group, the length and number of tails, the charge on the surfactant, the salinity of the solution, the temperature, and the flow conditions [9,13]. We are most interested in wormlike micelle because, as suggested by their pseudonym "living polymers," wormlike micelles display many of the same viscoelastic properties of polymers. However, although both wormlike micelle solutions and polymer solutions can be viscoelastic, wormlike micelles are physically quite different from polymers. Whereas the backbone of a polymer is covalently bonded and rigid, wormlike micelles are held together by relatively weak physical attractions and as a result are continuously breaking and reforming with time. In an entangled network, both individual polymer chains and wormlike micelles can relieve stress through reptation driven by Brownian motion [10]. However, unlike polymeric fluids, wormlike micelle solutions have access to a number of stress relief mechanisms in addition to reptation. Wormlike micelles can relieve stress and eliminate entanglement points by either breaking and reforming in a lower stress state [11] or alternatively by creating a temporary branch point which

allows two entangled micelles to pull right through each other, thereby eliminating the entanglement point and relieving stress in what has become known as a ghostlike crossing [14]. Additionally, the constant reorganization of the network structure results in several interesting phenomena when subjected to strong flows. Under all but the most extreme conditions, these solutions' large viscosities lead to a vanishingly small Reynolds number $\mathrm{Re} = \rho U L/\mu$, where ρ is the fluid density, U is the flow velocity, L is the characteristic length scale, and μ is the fluid viscosity. In all of the experiments presented in this work, the Reynolds number is of order 10^{-4}.

An interesting feature of wormlike micelles is their mechanism of mechanical failure under an applied stress. Flow curves have shown these solutions to be shear thinning [11] and strain hardening [15], however these two non-Newtonian behaviors do not predict their method of failure. In extensional flow, wormlike micelles demonstrate considerable strain hardening in the extensional viscosity with increasing accumulated strain. In some instances, the extensional viscosity η_E of wormlike micelle solutions has been found to be more than 1000 times the shear viscosity η_0. Above a critical extension rate, the filament stretching extensional rheology measurements of wormlike micelle solution were observed to come to an abrupt end with rupture of the fluid filament near its axial midplane. This behavior has been observed most recently by Bhardwaj *et al.* [12] and is believed to be caused by a scission of individual micelle chains. This type of dramatic failure can manifest itself as instabilities in not just extensional flows, but complex flows as well. For example, the flow around a sphere contains regions of shear as the fluid passes around the circumference, as well as extension in the wake of the sphere. Given that the fluid is known to be shear thinning as well as extensionally thickening, the combination of these qualities and the complex flow field yields some interesting results. Chen and Rothstein [16] observed that above a critical Deborah number a class of elastic instabilities occurred that was related to the rupture of these micellar solutions in the extensional flow present in the wake of a sphere. By measuring the flow fields with particle image velocimetry (PIV) and flow-induced birefringence (FIB) they were able to explore the kinematics of the flow. The flow of wormlike micelle solutions past a single cylinder or an array of circular cylinders has also been shown to become unstable [17,18]. Measurements of velocity profile were performed using PIV over a wide range of Deborah numbers. The PIV measurements showed large velocity gradients around the equator of the cylinder and a strong extensional flow downstream of the cylinder. Beyond a Deborah number of $\mathrm{De} = 4.5$, pressure drop measurements were observed to fluctuate in time with an amplitude that increased with increasing Deborah number. The fluctuations initially appeared to be time periodic with a frequency of approximately 1 Hz. At the highest Deborah numbers studied the fluctuations were no longer periodic, but instead appeared to be chaotic. The instability was confirmed through PIV and FIB measurements. As the Deborah number continued to increase, the micelle rupture events that lead to the elastic instability appeared to transition from a global to a localized instability and distributed axially in the wake of the circular cylinder. Similar instabilities have also been observed in [19,20].

B. Newtonian fluid-structure interactions

Vortex-induced vibration (VIV) of a flexibly mounted rigid cylinder with a circular cross section placed in fluid flow and free to oscillate in the crossflow direction, i.e., the direction perpendicular to the oncoming flow, has become a canonical problem in fluid-structure interaction (FSI) studies. Work by several investigators has helped elucidate the fundamentals of VIV [21–28]. Large-amplitude oscillations occur when the frequency of vortex formation is relatively close to the natural frequency of the structure. Then the frequency of vortex shedding can be entrained and become equal to the frequency of the structural crossflow vibrations. This wake-body resonance condition is referred to as lock-in. Substantial differences exist when the rigid cylinder is also allowed to move in the in-line direction, the direction parallel to the oncoming flow [29,30]. Inclusion of the in-line motion leads to significant changes in hydrodynamic forces acting on the rigid cylinder, depending on the phase difference between the in-line and the crossflow vibrations [31,32].

The case of a long flexible cylinder in a crossflow has been considered only recently due to its complexities. These complexities are associated with the distributed interaction between the fluid and the flexible body, including the difficulty to pinpoint the region where the fluid excites the body and identifying the mechanisms of energy redistribution along the span. Detailed laboratory experiments on flexible structures placed in flow have provided information on the amplitude of vibration, excited frequencies, and structural wave numbers [33,34]. For long flexible cylinders, contrary to the case of rigid cylinders, the phase difference between the in-line and crossflow displacements can vary along the span, leading to diverse trajectories along the structure [35–37]. A dominant mechanism has been identified in the interaction between a flexible cylinder undergoing VIV in sheared crossflow and the vortices forming in its wake: Energy is transferred from the fluid to the body under a resonance condition, which occurs within a well-defined region of the span, dominated by counterclockwise figure-eight orbits [31]. In all the cases described above, the fluid was Newtonian and the flow was at moderate to high Reynolds numbers $\mathrm{Re} > 50$. In these inertial-dominated flows, the motion of the cylinder was driven by the shedding of vortices which separate from the cylinder and are shed. There is, however, a whole class of non-Newtonian flows (as discussed in Sec. I A) in which the Reynolds number is vanishingly small and inertia plays essentially no role and yet the flow can become unstable. In these cases, the presence of high-molecular-weight polymers or wormlike micelles can make the fluids elastic. The combination of fluid elasticity and mean curvature of the streamlines has been shown to destabilize the flow and lead to the onset of elastically driven flow instabilities [38].

C. Viscoelastic fluid-structure interactions

Viscoelastic fluids such as polymer melts and solutions, micelles solutions, and suspensions are encountered in a variety of industries and applications critical to modern day economics. A fundamental understanding of how these viscoelastic fluids interact with structures can have significant influence on a number of very different applications ranging from polymer processing to health care. In our previous work, we showed that elastic instabilities occurring in a flow of viscoelastic wormlike micelle solution can induce motion in a flexible structure placed in its flow path [39]. In that particular study, a flexible rectangular sheet was placed at various inclinations to a flow of wormlike micelle solution. Beyond a critical flow velocity, at which the wormlike micelle solution became unstable, the flexible sheet underwent periodic oscillations in line with the flow direction. The amplitude of these oscillations was found to increase to a maximum and then decay with increasing flow velocity while the frequency of oscillations increased monotonically with increasing flow velocity. The time histories of these oscillations followed a sawtooth pattern which was coupled with the elastic instabilities occurring in the flow. The time variation of the structural deformation and the state of stress in the flow field were presented using bright field and FIB images. Due to the low flexural rigidity of the flexible sheet, under flow conditions, the cross section of the sheet was observed to bend into a complex C shape that was dependent on the inclination of the flexible sheet with respect to the flow direction and also varied along the span of the flexible sheet. This complex shape made the structure's response highly nonlinear and challenging to predict. In this paper a much simpler flexible structure of a circular cross section is placed in the flow of a wormlike micelle solution, thereby ensuring that the cross section remains undeformed under flow conditions. From the experiments presented here, we will show that the complex deformation of the flexible sheet is not necessary for viscoelastic fluid-structure instabilities to be observed. Additionally, the use of a circular cylinder makes it possible to directly compare our results with a number of Newtonian fluid-structure interaction studies in the literature.

II. EXPERIMENTAL SETUP

A. Cylinder properties

A schematic diagram of the experimental setup is shown in Fig. 2. The flexible circular cylinder made of polydimethysiloxane was fabricated using a 40:1 volume ratio of the base and curing agent

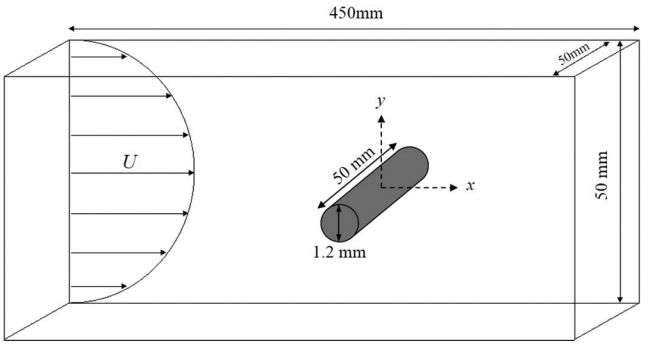

FIG. 2. Schematic diagram of the experimental setup.

from a Sylgard-184 silicone elastomer kit (Dow Corning). The mixture was first degassed in a vacuum chamber and then slowly filled into a glass capillary tube and left to cross-link. After the mixture had cured, the glass tube was cracked open to dislodge a flexible cylinder with a diameter of 1.2 mm. The cylinder used in the experiments presented here was tested to have an elastic modulus of 0.5 MPa and a natural frequency of 1.4 Hz inferred from a pluck test when immersed in the viscoelastic fluid used here. The flexible cylinder was then mounted transversally at the center of a rectangular acrylic channel with a cross-sectional area of 50 mm^2 and a length of 450 mm. The ends of the cylinder were sealed with a 10:1 volume ratio of the base from the Sylgard-184 kit and 25–30% methylhydrosiloxane-dimethylsiloxane copolymer (HMS-301 Gelest Inc.). This mixture cured quickly while holding the flexible cylinder in place and also provided an easily replaceable seal. The tension in the flexible cylinder was provided solely by the weight of the cylinder and was calculated to be 0.7×10^{-3} N. A positive displacement pump controlled by a linear motor was used to drive the fluid with minimum pressure fluctuations [18]. The flow velocity was calculated from the known values of the piston displacement rate and cross-sectional area of the piston and flow cell. The piston motion was controlled with addressable microstaging, capable of a flow rate resolution of 4 mm^3/s. The flow velocity was varied from 0 to 11.5 mm/s in this study. The range of flow velocities was limited at the higher end by the capacity of the system and thus the measurement time available for the artifacts of the experimental startup to die out.

B. Structural deformation tracking

In order to quantitatively measure the deformation of the flexible cylinder during the flow of the test fluid, discrete points were marked along the length of the cylinder. During the test, the motion of the flexible cylinder was captured using a high-speed camera (Phantom v4.2), recording videos at 100 frames/s (fps). The captured high-resolution videos were then used as an input in a tracking software (Tracker), which located and tracked the motion of discrete points and provided the displacement time histories at each point for each frame. In this study, the flexible cylinder showed only the first mode of excitation in its oscillations. Therefore, only the midsection point on the cylinder was input into the tracking software and this was sufficient to gain information regarding the amplitude and frequency of oscillations. For each time history, a minimum of 180 s of data was collected, once the flexible cylinder reached a steady state.

C. Fluid rheology

1. Sample preparation

The test fluid was composed of wormlike micelle solution assembled from 50 mM of cationic surfactant cetyltrimethylammoniun bromide (CTAB) (MP Biomedicals) and 25 mM of sodium salicylate (NaSal) (Fisher Scientific) in deionized water. This solution is well above the critical

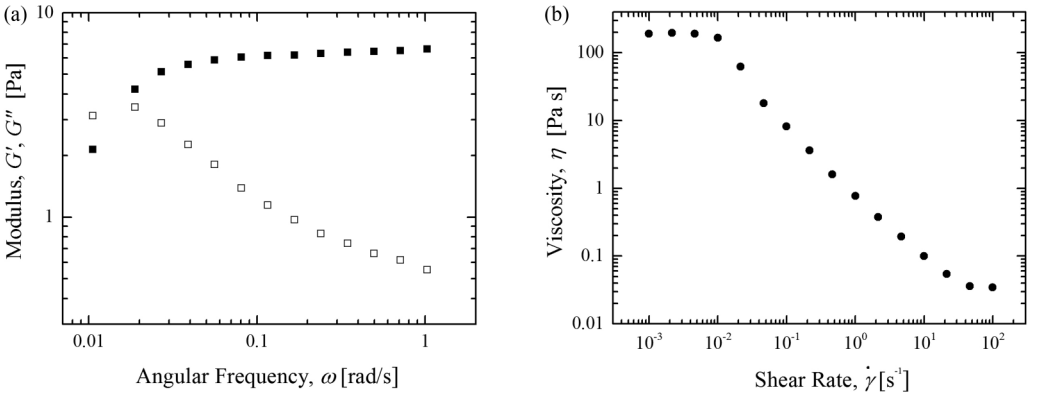

FIG. 3. Steady and dynamic shear rheology data of the 50 mM CTAB, 25 mM NaSal wormlike micelle solution $T_{\text{ref}} = 25\,^{\circ}\text{C}$: (a) the storage modulus G' (■) and the loss modulus G'' (□) as a function of frequency and (b) the viscosity as a function of shear rate.

micelle concentration, which for CTAB in pure water has a CMC of 0.9 mM and is again significantly lower in the presence of salt [9]. The CTAB was dissolved in aqueous NaSal solution on a hot plate with a magnetic stirring bar. During mixing, a moderately elevated temperature was applied to reduce viscosity and aid in uniform mixing. After the solutions were fully dissolved, approximately 20–30 min, they were allowed to settle at room temperature for at least 24 h before any experiments were performed to allow air bubbles introduced during mixing to rise out of the solution. At the concentrations used, the wormlike micelle solution is concentrated and entangled with a significant number of entanglement points per chain [9]. When analyzing and presenting the experimental data, the relaxation times and viscosities were adjusted to their values at a reference temperature of $T_{\text{ref}} = 25\,^{\circ}\text{C}$ using time-temperature superposition with a shift factor a_T defined by the Arrhenius equation [40]. Within the temperature range of our experiments, the Arrhenius form of the time-temperature superposition shift factor was found to be in good agreement with the rheological data for each of the wormlike micelle solutions tested. However, because of the sensitivity of the underlying wormlike micelle structure to temperature, every effort was made to maintain the fluid temperature at 25 °C within plus or minus a few tenths of a degree for all of the experiments presented herein.

2. Shear rheology

The steady and dynamic shear rheology of the test fluid was characterized using a stress-controlled rheometer (TA instruments, AR2000) with a 6 cm diameter and 2° cone geometry. The micelle solution was loaded and allowed to equilibrate for several minutes. The samples were not presheared. In Fig. 3(a), the storage modulus G' and loss modulus G'' of the CTAB-NaSal wormlike micelle solutions are plotted as a function of angular frequency ω. The CTAB-NaSal solution has a Maxwell relaxation time of $\lambda = 47$ s and a zero shear viscosity of $\eta_0 = 200$ Pa s at $T = 25\,^{\circ}\text{C}$. The deviation of the rheological data from the predictions of a single-mode Maxwell model observed at large angular frequencies in Fig. 3 corresponds to the Rouse-like behavior of the micelle between entanglement points [41] and can be used to determine both the breakup time λ_{br} and the reptation time λ_{rep} of the wormlike micelle chains. In the fast breaking limit $\lambda_{\text{rep}} \ll \lambda_{\text{br}}$, Cates showed that the breakup and reptation time could be related to the measured value of the Maxwell relaxation time through $\lambda = \sqrt{\lambda_{\text{br}}\lambda_{\text{rep}}}$ [42]. Additionally, the theoretical mesh size $\zeta_m = (kT/G_0)^{1/3}$ [43,44] can be determined in order to gain some information about the proximity of entanglement points and the density of the wormlike micelle mesh. The wormlike micelle solution used in this study has breakup and reptation times of $\lambda_{\text{br}} = 2$ s and $\lambda_{\text{rep}} = 52.6$ s, respectively, and theoretical mesh size of 8.6×10^{-9} m. In Fig. 3(a), the steady shear viscosity η is plotted as a function of shear rate $\dot{\gamma}$.

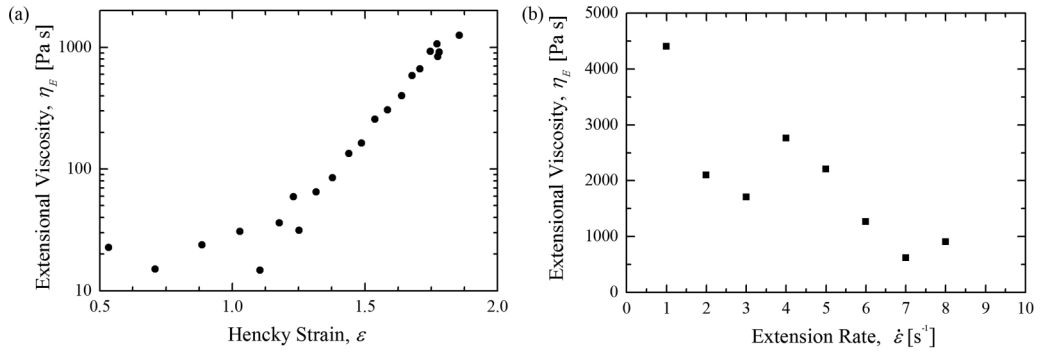

FIG. 4. (a) Representative plot of transient filament stretching rheometry experiments for the 50 mM CTAB, 25 mM NaSal wormlike micelle solution at Wi = 288. The symbols represent the elastic contribution to the tensile stress difference as a function of Hencky strain. The experiment ends abruptly upon the rupture of the fluid filament. (b) Maximum extensional viscosity reached before filament rupture as a function of strain rate for the 50 mM CTAB, 25 mM NaSal wormlike micelle solution.

At small shear rates and angular frequencies, the micelle solutions have a constant zero shear rate viscosity. As the shear rate is increased, the fluid begins to shear thin. At a critical shear rate, the viscosity drops precipitously approaching, but not reaching, a slope of $\eta \propto \gamma^{-1}$.

3. Extensional rheology

Wormlike micelle solutions have been the subject of many experiments in extensional flow in recent years [12]. A filament stretching extensional rheometer capable of imposing a homogeneous uniaxial extension rate $\dot{\varepsilon}$ on a fluid filament placed between its two end plates was used to make simultaneous measurements of the evolution in the force and the midpoint radius R_{mid}. The transient extensional viscosity η_E may be extracted from the principle elastic tensile stress and is often nondimensionalized as a Trouton ratio $\text{Tr} = \langle \tau_{zz} - \tau_{rr} \rangle / \eta_0 \dot{\varepsilon} = \eta_E / \eta_0$, where $\langle \tau_{zz} - \tau_{rr} \rangle$ is the principal elastic tensile stress difference generated within the fluid filament. The deformation imposed upon the fluid filament can be described in terms of a Hencky strain $\varepsilon = 2ln(R_{\text{mid}}/R_0)$, where R_0 is the initial midpoint radius of the fluid filament. The strength of the extensional flow is characterized by the Weissenberg number $\text{Wi} = \lambda \dot{\varepsilon}$, which is the product of the characteristic relaxation time of the fluid λ and the extension rate $\dot{\varepsilon}$. The Weissenberg number is a measure of the relative importance of elastic to viscous stresses in a flow. For a detailed description of the extensional rheometer used in these experiments see Ref. [15].

The extensional rheology of the solution tested was previously investigated and published by Bhardwaj *et al.* [12,45] and Rothstein [15]. However, for completeness, filament stretching experiments were conducted for the test fluid used in this study. A representative plot of the extensional viscosity η_E of the 50 mM CTAB, 25 mM NaSal as a function of Hencky strain for a Weissenberg number of Wi = 288 is presented in Fig. 4(a). The elastic tensile stress is found to increase monotonically with increasing Hencky strain, demonstrating reasonably a strong strain hardening by achieving a final elastic tensile stress of $\triangle \tau_e = 7.5$ kPa at $\varepsilon \cong 1.8$. At large extension rates $\text{Wi} \gg 1$, the fluid filaments were all found to rupture. For all of the experiments that ended with a filament rupture, the final maximum elastic stress that was achieved in the fluid filaments of each solution was found to be roughly constant, independent from the extension rate [12]. Owing to the constant elastic tensile stress, the extensional viscosity is found to decrease linearly with increasing imposed extension rate $\eta_E \propto \dot{\varepsilon}^{-1}$ as can be seen in Fig. 4(b). It has been hypothesized that the tensile stress of rupture corresponds to the maximum stress that the micelles can withstand before they begin to fail en masse [15]. The dynamics of the filament rupture has been captured with high-speed photography in the past and the interested reader is referred to Ref. [16] or [12] for details. This

failure of the micelles in extensional flows has also been shown to result in elastic flow instabilities in complex flows like those past spheres [16], cylinders [17], and sheets [39].

D. Flow-induced birefringence

The refractive index of a wormlike micelle varies depending on whether the light passes parallel or normal to the micelle's backbone. By passing light of a known polarization state and frequency through a fluid sample and measuring the resulting change in polarization state, flow-induced birefringence takes advantage of this fact to measure the deformation of the micelle. Under all flow conditions, this technique can at least qualitatively elucidate the regions of large stress in a flow. In the limit of small deformations, an optical train can be built up using Mueller calculus and a value of the micellar deformation can be calculated from a stress-optic coefficient. Flow-induced birefringence measurements have been used quite extensively to examine both steady and transient flows of wormlike micelles [16,46–49]. A white light source was used to illuminate the flow between crossed polarizers. The polarizers were oriented at 45° and 135° to highlight the regions of extensional deformation. It is known that in flows with stagnation points, a narrow region of high polymer or micelle deformation known as birefringent strands can form in the strong extensional flow just downstream of the stagnation point [50,51]. These birefringent strands appear as bright areas or fringes directly in the wake of the flexible sheet. These fringe patterns are in excellent agreement with the patterns observed in both experiments [52] and numerical simulations [53,54]. In our study, the birefringence quickly goes through orders, here seen as rainbow fringe patterns, indicating a substantial amount of deformation and thus stress accumulated by the fluid. A Nikon D70 digital camera was used to capture the birefringent patterns in the wormlike micelle solution generated by the flow for each linear polarizer configuration. Due to the extreme deformation that the micellar network undergoes at high Deborah numbers, data analysis becomes impractical. As such, for the purpose of this study, the full field FIB technique is used only qualitatively to highlight the deformation; it is a visualization tool to aid the observer.

E. Particle image velocimetry

Particle image velocimetry was used to generate a complete and quantitative measurement of the velocity flow field around the flexible cylinder. The wormlike micelle solution was seeded with silver-coated glass spheres (Potters Industries) at 0.005% by weight and allowed to equilibrate in the test geometry for 24 h. Although the tracer particles are denser than the surrounding fluid, because of the high viscosity of the micelle solution and the small size of the seed particles, their settling time was calculated to be on the order of months. A measurement plane approximately 90 mm in length and 1 mm in width and coinciding with the centerline of the sphere was illuminated with a laser light sheet formed by passing a 500-mW argon laser (National Laser 458–514 nm) through a cylindrical lens. This lens and fiber optical train used allowed velocity profile measurements over the full channel height. The light scattered from the tracer particles was captured with a high-speed camera (Allied Vision) at 80 fps with a resolution of 1280×1024 pixels^2 and broken into a sequence of digital images using Adobe Media Encoder. The image sequence was then processed using LaVision's PIV software. Length scale and velocity measurements were made by measuring the flexible cylinder size in the field of view of the camera.

III. RESULTS AND DISCUSSION

A. Dynamic response of the flexible cylinder

By measuring the midsection displacement of the flexible cylinder for a range of flow velocities from 0 to 11.5 mm/s, a number of interesting phenomena began to appear. For the range of flow velocities tested, the Reynolds number was on the order of 10^{-4}. As a result, these experiments were in the Stokes flow regime and inertial flow effects could be neglected. In Fig. 5, the effects of increasing flow velocity on the x and y midsection displacements of the flexible cylinder are

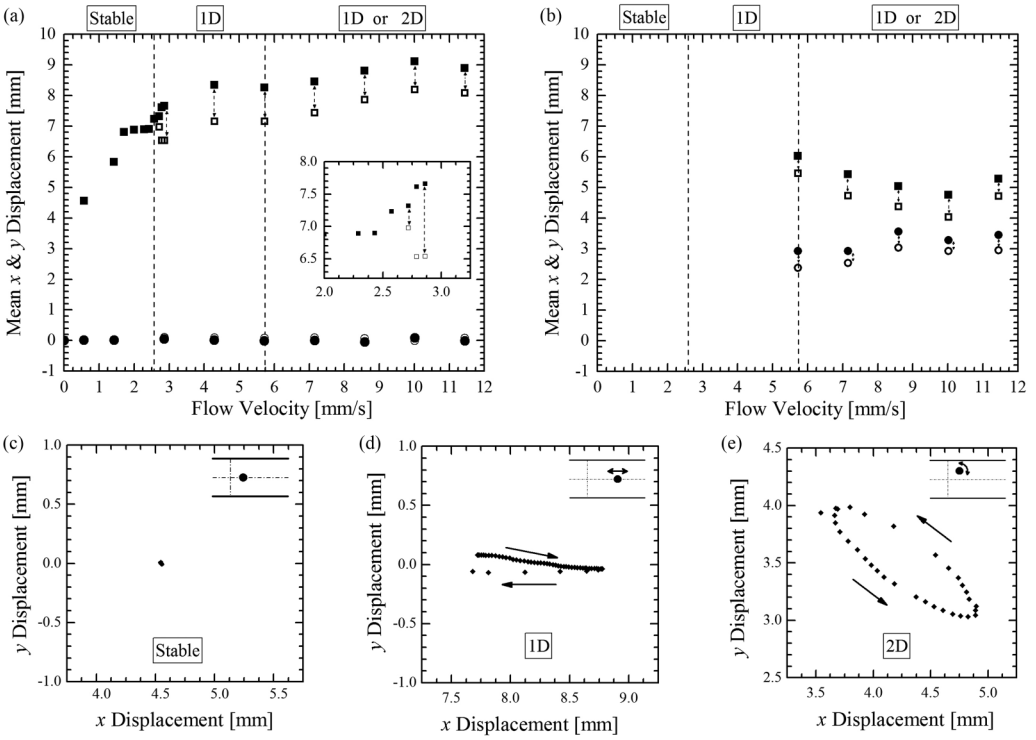

FIG. 5. (a) and (b) Displacements x (■) and y (●) of the flexible cylinder for the range of flow velocities tested. Note that (a) represents data only for 1D oscillations of the cylinder and (b) represents just the 2D oscillations of the cylinder. The closed and open symbols represent the mean maximum and minimum positions during cylinder oscillations, respectively. The inset in (a) shows a close-up of cylinder displacement at the critical velocity for the onset of cylinder oscillations. The path followed by the flexible cylinder is shown during its (c) stable, (d) unstable 1D, and (e) unstable 2D oscillations at $U = 4.3$, 10, and 11.5 mm/s, respectively.

shown. The flexible cylinder started out undeflected at zero flow velocity. As the flexible cylinder was subjected to flow velocity up to $U_{\text{crit}} = 2.7$ mm/s, it was displaced into the flow direction. This resulted in a static in-line x displacement and stable crossflow y displacement as shown in the stable region in Fig. 5(a). In the xy plane, this static displacement appeared as a single point as shown in Fig. 5(c). At flow velocities beyond $U_{\text{crit}} = 2.7$ mm/s, the fluid flow was no longer stable and instead began to undergo elastic instabilities, which greatly affected the response of the flexible cylinder. This corresponds to a Weissenberg number of $\text{Wi}_{\text{crit}} = 106$. This value is larger than the critical Weissenberg number for the onset of elastic instabilities for flow past an undeformed or rigid cylinder [18]. For these flow velocities, the flexible cylinder began to undergo oscillations. In Figs. 5(a) and 5(b), the flow regimes beyond the stable regime have been divided into two regions, namely, one where only 1D oscillations have been observed and another, starting at $U_{\text{crit}_{2D}} = 5.7$ mm/s, where both 1D and 2D oscillations have been observed for a specific flow velocity. This critical velocity corresponds to a Weissenberg number of $\text{Wi}_{\text{crit}_{2D}} = 223$.

In Fig. 5(a), the mean x and y displacements of the flexible cylinder occurring during the 1D oscillations have been plotted with increasing flow velocity. The closed and open points represent the mean maximum and minimum positions of the flexible cylinder during its oscillation at a given flow velocity. In this 1D oscillation, the mean maximum and minimum x displacements are nonzero and different from each other in the x direction while they are very close to each other in the y direction. The representative xy profile at $U = 4.3$ mm/s for the 1D type of oscillation is shown in Fig. 5(d), where the displacement increased steadily for 6.7 s in the x direction followed by a rapid decrease in

the x displacement in 0.75 s. During this single-oscillation cycle, the y displacement stayed almost constant as compared to the x displacement. Due to this straight-line pattern of oscillation, this type of response of the flexible cylinder has been termed a 1D oscillation. The x displacement of the 1D oscillation reached a plateau at flow velocities beyond $U = 4.3$ mm/s.

In Fig. 5(b), the mean x and y displacements of the flexible cylinder have been plotted with increasing flow velocities for the 2D oscillations. In these 2D oscillations, the position of the flexible cylinder is no longer in line with the flow direction and instead follows an elliptical trajectory. A representative xy displacement profile at $U = 11.5$ mm/s is shown in Fig. 5(e). As both the mean x and y displacements of the flexible cylinder become essential in a 2D oscillation, the flexible cylinder can be seen to trace an ellipsoidal path during a single oscillation. The side of the ellipse where the oscillation began is slow, taking up to 1.25 s, followed by the other quicker side, which occurs in 0.15 s. Both the x and y displacements show a similar amplitude unlike that seen for the 1D oscillations. The 2D oscillations were observed to occur on either side of the flow cell and were not confined to any dominant half.

The x and y displacement time histories and xy plane displacements of the flexible cylinder have been plotted at sample flow velocities of $U = 4.3$, 10, and 11.5 mm/s in Fig. 6. At $U = 4.3$ mm/s, the flow velocity is beyond U_{crit} and as a result, the flexible cylinder undergoes 1D oscillations with the y displacement staying around zero during the oscillations [Fig. 6(a)]. In the xy plane, the cylinder moves from its zero position and then remains in line with flow direction during oscillations. This sawtooth 1D oscillation was previously observed in viscoelastic fluid-structure interactions of a flexible sheet [39], which suggests that the character of these oscillations is due to the fluid flow and not altered by a change in the structure's shape or deformation. At $U = 10$ mm/s, the flexible cylinder started by moving in the in-line direction but was knocked off this position to rotate about its long axis to assume a new mean position. At this displaced position, the flexible cylinder underwent 2D oscillations as seen by the in-phase x and y displacements [$t = 10.20$ s in Fig. 6(c)]. However, this position did not continue to remain favorable and as a result, the flexible cylinder was observed to migrate back to its original in-line position over time. This return to the in-line position was slower than the path followed during the first change of position. This indicates that neither the 1D nor the 2D modes of instability were dominant at this flow velocity. However, as the flow velocity was increased, the 2D mode became more dominant and a similar return to symmetry was rarely obtained. Two-dimensional oscillations are shown in Fig. 6(e) for $U = 11.5$ mm/s. In this case, the flexible cylinder rotated about its long axis to assume a position for 2D oscillations and continued to remain there for the rest of the run.

The amplitude and frequency of flexible cylinder oscillations are plotted in Fig. 7. The 1D flexible cylinder oscillations were observed to start at $U_{\text{crit}} = 2.7$ mm/s as the wormlike micelle solution became unstable. The amplitude of oscillation reached a maximum of 1.2 mm (corresponding to a dimensionless amplitude $A/D = 1$), beyond which it decayed with increasing flow velocity. The frequency of these oscillations continued to grow monotonically with increasing flow velocity. The 2D flexible cylinder oscillations began at $U_{\text{crit}_{2D}} = 5.7$ mm/s and quickly reached a plateau with increasing flow velocity at 0.8 mm ($A/D = 0.67$). The amplitude of these oscillations consists of a vector addition of the x and y displacement components $A = \sqrt{(\Delta x)^2 + (\Delta y)^2}$. The frequency of these oscillations increased at a rate that is approximately half of the rate of increase in the frequency of 1D oscillations. As the natural frequency of the cylinder $f_N = 1.4$ Hz was found to be larger than the highest frequency of oscillations observed in the experiments, no lock-in region was observed for the system. However, if the natural frequency of the cylinder was modified or the oscillation frequency changed by choosing a different fluid with a lower relaxation time, lock-in might by observed for these systems.

B. Particle image velocimetry

Velocity vector fields were constructed using particle image velocimetry during the flexible cylinder oscillations in order to study the flow field during both cylinder displacements. Velocity

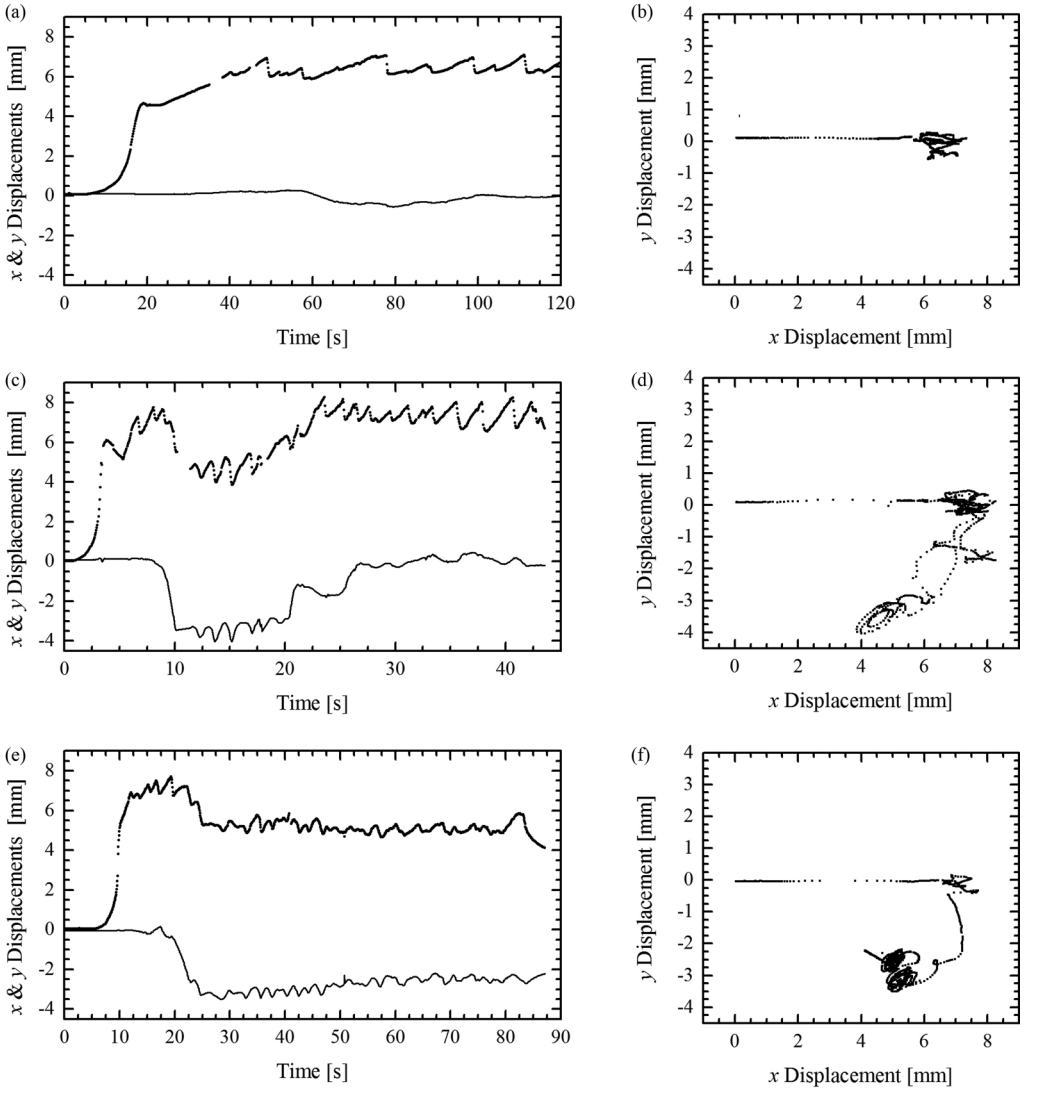

FIG. 6. (a), (c), and (e) The x and y displacements of the flexible cylinder plotted against time (dotted and solid lines respectively) and (b), (d), and (f) the xy displacement orbits at (a) and (b) $U = 4.3$ mm/s, (c) and (d) 10 mm/s, and (e) and (f) 11.5 mm/s. The sampling frequency is 8 Hz.

fields for a representative 1D oscillation cycle occurring at $U = 7.2$ mm/s are presented in Fig. 8 in a series of four images, taken at a time interval of $\Delta t = 0.06$ s. In the first image, the flexible cylinder is on its in-line deformation path while the wormlike micelle solution is flowing past it just prior to the onset of the elastic instability. At this moment, the cylinder appears to have reached a steady-state deformation induced by the flow. In the second image, the fluid downstream of the cylinder shows the onset of the viscoelastic flow instability resulting from the local breakdown of the wormlike micelle solution in the region of the flow with the largest extensional stress. At this moment, the micelles, which are under a significant elastic tensile stress in the wake of the cylinder, as shown in the birefringence images presented in the next section, have reached the maximum stress that can be supported. As the micelle network breaks down and the stored elastic energy is restored to the fluid resulting in a flow reversal downstream of the cylinder and a retraction of the cylinder to

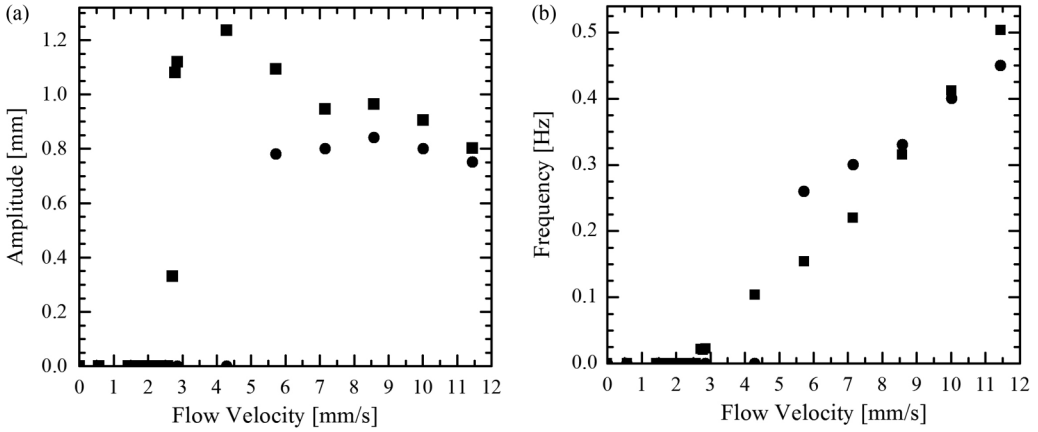

FIG. 7. (a) Amplitude and (b) frequency for 1D (■) and 2D (●) oscillations, plotted over the range of flow velocities tested.

a position back upstream. From the PIV, one can see a stagnation point developed just downstream from the cylinder, a jet of fluid forming downstream of the stagnation point, and two strong vortices forming between the jet of fluid and the walls of the flow cell. In all the PIV images, conservation

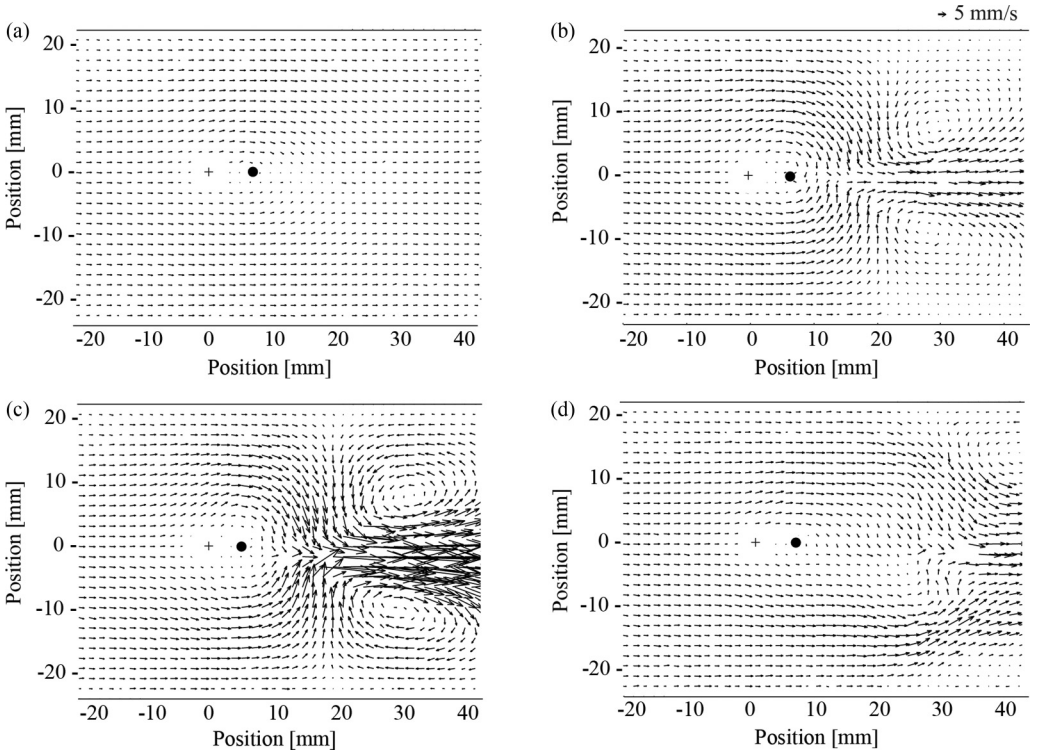

FIG. 8. Sequential PIV images of the flow around the flexible cylinder at $U = 7.15$ mm/s for a symmetric flow field. The + represents the position of the flexible cylinder at the start of a run while the ● represents the location of the cylinder within the flow field at the time of the oscillation. The flow is from left to right. Each image represents a time step of 0.06 s.

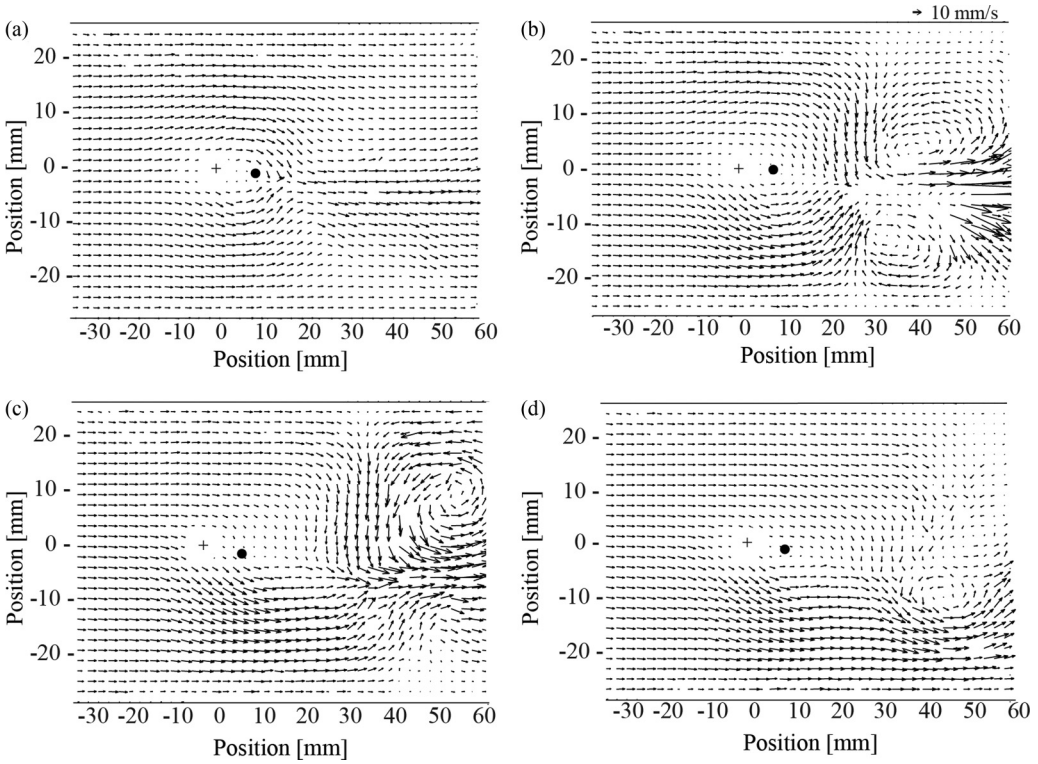

FIG. 9. The PIV image sequence of the flow around the flexible cylinder at $U = 11.5$ mm/s for an asymmetric fluid rupture in the flow field. The + represents the position of the flexible cylinder at the start of a run. The flow is from left to right. Each image represents a time step of 0.06 s.

of mass was checked and confirmed by integrating cross sections of the velocity profile in the y direction. Here the backflow of the vortex balances the increase in mass flux from the high-velocity jet to conserve mass in each snapshot in time. In the third image, there is an intensification of the fluid jet in the wake of the flexible cylinder and the vortices as the flexible cylinder recoils back sharply. This image is close to the maximum recoil rate for the cylinder as shown in the displacement versus time histories of Fig. 6(b). In the fourth image, the stagnation point, the high-speed jet and the vortices have convected downstream towards the end of the flow field visualized within this PIV image. At this moment, the flexible cylinder has completed its recoil path and is ready to start the next oscillation cycle with the flow of new undeformed wormlike micelle solution introduced from upstream.

In Fig. 9, a second 1D oscillation cycle occurring at $U = 11.5$ mm/s is illustrated through a series of four PIV vector fields taken $\Delta t = 0.06$ s apart. Unlike the 1D oscillations in Fig. 8 which were symmetric in y, with the oscillations all occurring at a cylinder position of $y = 0$, the oscillations at the higher velocity shown in Fig. 9 are one dimensional, but they are asymmetric. The oscillations in Fig. 9 occur along a line, but follow a path that is approximately 10° below the centerline of the flow cell. In the first image, the elastic flow instability can be seen to initiate just downstream of the flexible cylinder. Due to the asymmetry in the flow, the onset of the elastic flow instability results in an asymmetric flow response. The stagnation point appears to develop below the centerline of the channel, the jet forms at an angle to the horizontal axis, and the subsequent vortex formation shows the development of a stronger vortex towards the top of the channel. Rapid acceleration of the fluid occurs as seen in the second image while the flexible cylinder begins to recoil sharply. As the vortices are convected downstream, the exiting fluid in the third and fourth images maintains the

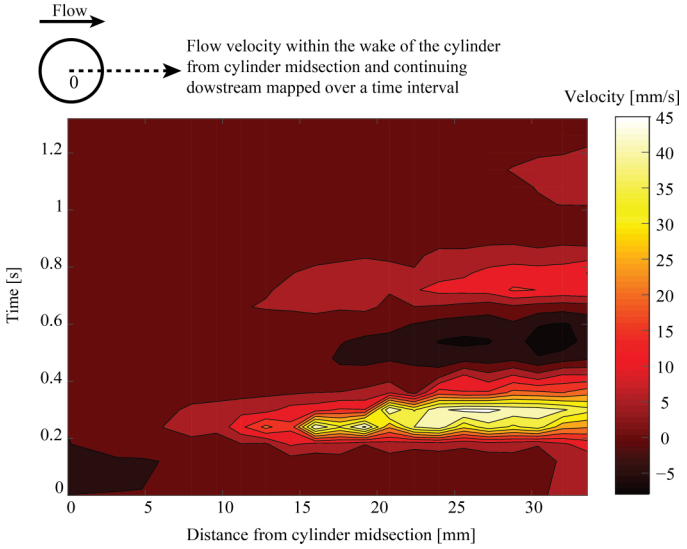

FIG. 10. Contour map of transient velocity vectors along the flow field centerline starting at the flexible cylinder center (0 mm) up to 35 mm downstream mapped over the start to the end of the sudden breakdown of wormlike micelle solution in the wake of the flexible cylinder at $U = 7.2$ mm/s.

asymmetry in the flow field. As the vortices convect downstream, the asymmetry in the jet can be observed to drive the vortex in the bottom half of the channel into the wall where it is quickly damped out, leaving only the vortex in the upper half of the channel having a positive vorticity behind to convect downstream. Note that this asymmetry in the elastic flow instability can occur either on the top or bottom of the downstream flow field. The amplitude of flexible cylinder oscillations decreases slightly at higher flow velocities where the oscillations are one dimensional but asymmetric. A cause of this asymmetric breakdown of fluid would be the shifting of the elastic flow instability from a global incident to a local one as the instability has been observed to occur at localized regions along the span of the cylinder instead of at the central midsection that was observed at low flow velocities. This transition was visualized through FIB for rigid cylinders [18] and was also observed for viscoelastic fluid-structure interactions of a flexible sheet [39].

The stages of the elastic flow instabilities that lead to rapid acceleration and deceleration of the fluid occurring in the wake of the flexible cylinder during a 1D oscillation have been illustrated using a contour map in Fig. 10 for the flow visualized in Fig. 8. The data are color coded to represent the magnitude of the fluid velocity along the centerline of the flow field from a point at $x = 0$ representing the center of the flexible cylinder to a distance $x = 35$ mm downstream. The y axis illustrates the variation of velocity with time starting at $t = 0$ where the cylinder is stretched to its maximum and running through a time interval of 1.3 s. This represents several cycles of the elastic flow instability and the cylinder oscillation. At $t = 0.25$ s, the elastic flow instability results in the formation of a strong jet 6 mm or roughly $5D$ downstream of the cylinder and the formation of a stagnation point just upstream of the jet. This was clearly observed in the PIV results of Fig. 8. What is interesting is that after the formation of the initial jet, the flow velocity behind the cylinder is found to oscillate between positive and negative with time. These oscillations are a clear manifestation of the elasticity and the recoverable elastic energy that is stored both in the structure and, more importantly, in the fluid itself. Similar effects were seen in the settling of spheres in these wormlike micelle solutions. After the micelle structure broke down and the sphere accelerated, it was seen to bounce up and down with time as if attached to an elastic band [16].

In Fig. 5, the flexible cylinder was shown to rotate about its long axis and shift from a deformed position that was in line with the flow direction to an off-the-centerline position. This caused a change

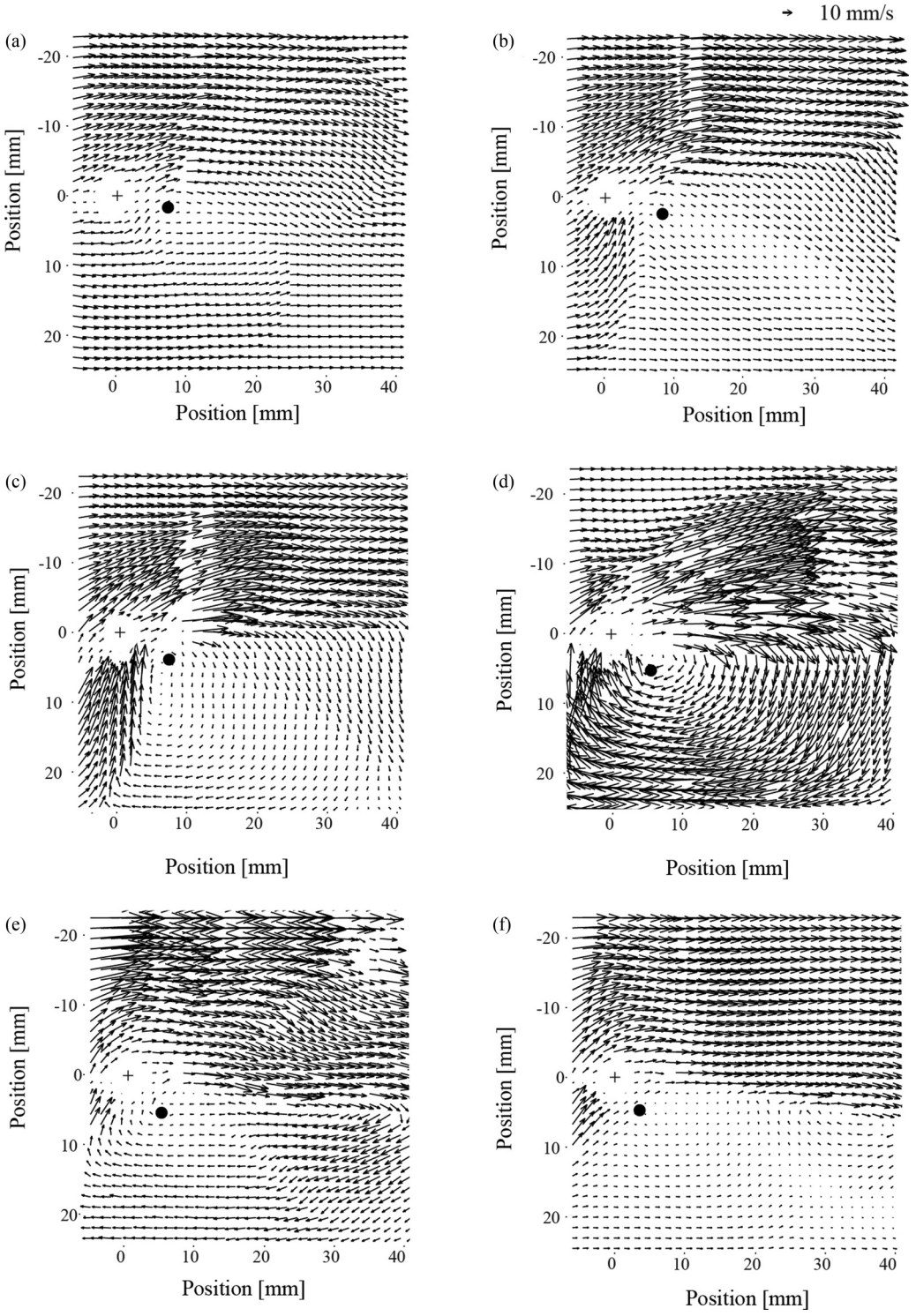

FIG. 11. The PIV image sequence of a 2D flexible cylinder oscillation at $U = 11.5$ mm/s. The + represents the position of the flexible cylinder at the start of a run. The flow is from left to right. Each image represents a time step of 0.06 s.

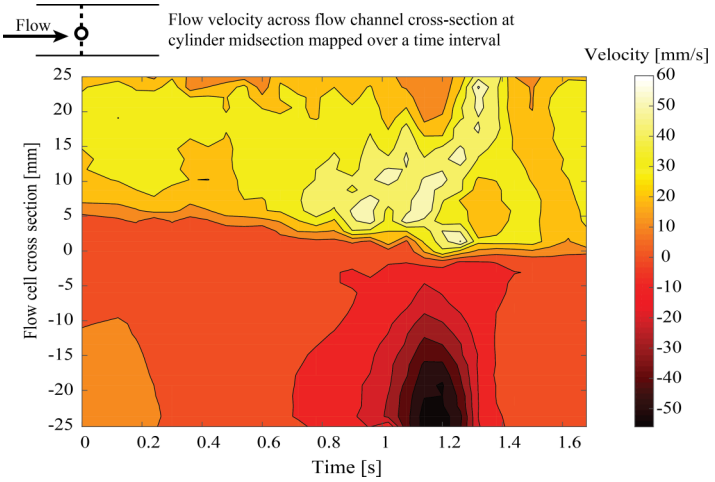

FIG. 12. Contour map of transient velocity vectors across the flow channel cross section taken at the cylinder midsection mapped over a time interval during the dramatic flow transition shown in Fig. 11 at $U = 11.5$ mm/s.

in the pattern of x and y displacements of the flexible cylinder leading to a 2D oscillation about this new position. The process of the cylinder rotating about its long axis to reach a new position is illustrated in a set of velocity vector field images collected at $U = 11.5$ mm/s, each taken in a time interval of 0.06 s and also in a contour map of the flow velocity across a slice of the flow channel at the flexible cylinder midsection. In Fig. 11(a), the flow field is asymmetric with the flexible cylinder stretched at a slight declination to the flow direction. This asymmetry is typical for oscillations observed at these higher flow velocities. The degree of asymmetry in the flow field continued to grow with time as the flexible cylinder can be seen to move further from the centerline of the flow cell. When the cylinder approaches a y displacement of $y = 2.5$ mm, a dramatic flow transition very different from the 1D oscillations is observed. At this point, the flow transitions from one which is roughly equally distributed over the top and bottom of the cylinder to a flow that only moves over the top of the cylinder. Below the cylinder, the flow is completely blocked by the presence of the cylinder. A slice of velocity vector fields at the cylinder midsection across the flow channel has been mapped in a contour map in Fig. 12 for the time duration of the PIV images shown in Fig. 11. What is amazing is that the cylinder is roughly $\frac{1}{40}$ the size of the channel and the degree of asymmetry represents only a 2.5% difference in the channel cross section available to the flow over or under the cylinder, yet it is enough to cause a profound effect on the flow. As can be seen in Fig. 11, the region of fluid below the flexible cylinder is almost stationary with a velocity that is at least ten times smaller than the velocity of the fluid over the cylinder. Just upstream of this stationery region, the flow is observed to deflect vertically and accelerate, almost as if flowing around a solid obstacle even though there is none. A weak recirculation is observed in the stationery region set up by the high-speed regions of fluid passing around it; however, the weak strength of the recirculation and the very large shear rates along its borders suggest the presence of shear bands [55]. The flow of the fluid concentrated over upper half of the flow field still leads to an extensional deformation of the fluid which in turn leads to a similar elastic instability in the wormlike micelle solution. As observed previously, the elastic flow instability leads to a sudden local acceleration of the fluid and a recoiling of the cylinder. At the same time, the flow field in this case is even more highly asymmetric. The jet of fluid is so strong that it can be seen in Fig. 11(d) to induce a backflow of fluid through the stationary region with a negative velocity that is more than five times the mean flow velocity upstream of the cylinder. The induced flow can be seen to cause the cylinder to rotate about its supports and reach a position with less x displacement, but a greatly enhanced y displacement as shown in Fig. 9(d). In

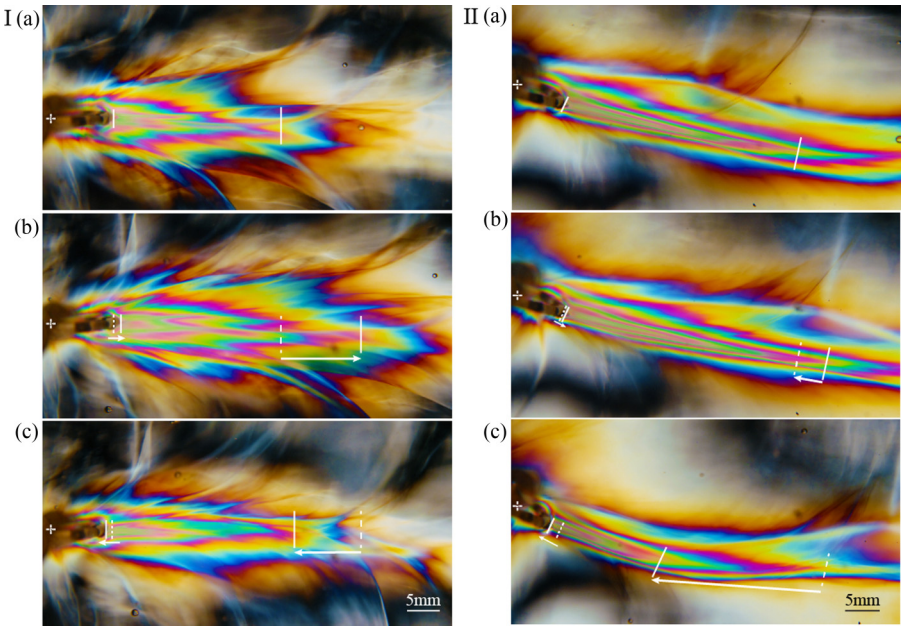

FIG. 13. The FIB images for two types of flexible cylinder oscillations observed. (I) At $U = 7.2$ mm/s, the flow field is symmetric and (II) at $U = 11.5$ mm/s, the flow field is asymmetric when (a) the flexible cylinder has reached maximum deflection, (b) the wormlike micelle solution fractures, causing the cylinder to recoil, and (c) the cylinder has reached the minimum position. The + represents the position of the flexible cylinder at the start of a run. The flow is from left to right.

Figs. 11(e) and 11(f), the flow field transitions back to the original highly asymmetric state as the stationary zone is slowly recovered before the onset of another flow instability.

C. Flow-induced birefringence

The flow-induced birefringence technique described in Sec. II D was used to qualitatively examine the transition of extensional stresses in the wormlike micelle solution during each flexible cylinder oscillation. Figure 13 has been divided into two sections, I and II, highlighting the two types of oscillation cycles. In Fig. 13I(a), the flexible cylinder can be seen as to be stretched parallel to the flow direction with a bright birefringent tail in its wake. This birefringent tail grows in length and size along with an increase in x displacement of the flexible cylinder in Fig. 13I(b). In Fig. 13I(c), the wormlike micelle solution has broken down, resulting in the onset of the elastic flow instability. This can be seen by the large drop in the length and size of the birefringent tail in the wake of the cylinder. The flexible cylinder at this point has also sharply recoiled, leading to an end of an oscillation cycle. In part II of Fig. 13, the flexible cylinder has rotated off of the central position and is instead stretched diagonally downward in the lower half of the flow field. In Fig. 13II(a), the birefringent tail can be seen in the wake of the flexible cylinder, however it is much flatter than the tail seen in case I due to the birefringent region being present in the upper region of the fluid where the flow was much faster, as seen in the PIV images (Fig. 11). This birefringent tail again grows in length and size to reach a maximum beyond which the flexible cylinder could not be stretched further by the wormlike micelle network [Fig. 13II(b)]. As the wormlike micelle network breaks down, it releases some of the stress deforming the flexible cylinder and allows it recoil backward. In Fig. 13II(c), the recoiled flexible cylinder has a much smaller birefringent tail which will again start its cycle of growth and decay in the next cycle of oscillations. An interesting feature of this two-dimensional type of oscillation is that there is no birefringence or extensional stress developed in the pocket of fluid that remains

locked in the lower wake region of the flexible cylinder throughout the entire oscillation cycle. The fast-moving fluid in the asymmetric flow field is the portion of the wormlike micelle solution that is responsible for the deformation of the flexible cylinder. The large birefringent and velocity gradients observed at the borderline between the fast-moving and slow-moving zones is strongly suggestive of the presence of a shear band in the micelles [55,56]. How or why it develops in the center of the flow channel is a bit of a mystery.

In order to understand the complex 2D flow instability observed at high Weissenberg numbers, we turn to a number of recent studies of the flow of viscoelastic polymer solutions past rigid cylinders [57–60]. For flow of a viscoelastic polymer solution around a confined circular cylinder, a series of elastic instabilities was observed to occur. The form of the viscoelastic flow instabilities for a polymeric fluid flowing around a rigid stationary cylinder are quite different from those observed for wormlike micelle solutions. This instability is not found to originate with a fluid rupture in the wake as it is for the wormlike micelle solutions. For viscoelastic fluids that do not shear thin, so-called Boger fluids, a spatially periodic cellular structure distributed along the wake of the cylinder was observed [60]. This cellular structure was initially stable with time, but was found to become time dependent with increasing Weissenberg number. For shear thinning polymeric fluids, a different form of the viscoelastic flow instability was observed. For these fluids, a break in the symmetry of the flow was observed upstream of the cylinder along the stagnation streamline [57]. This asymmetric flow was found to lead to a time-dependent flow that can be observed downstream of the cylinder and eventually, at high enough flow strengths, to a flow separation upstream of the cylinder.

Following the work of McKinley *et al.* [60], Shi *et al.* showed that the difference in these two classes of flow instability could be understood using the elastic Mach number [58]. In terms of the elastic Mach number, $\mathrm{Ma}_e = \sqrt{\mathrm{Re}\,\mathrm{Wi}} = U/\sqrt{\eta/\rho\lambda}$ [61], where U is the flow velocity, η is the shear-rate-dependent viscosity with the shear rate calculated as $\dot{\gamma} = U/(H/2)$ with H the flow cell width, ρ is the fluid density, and λ is the fluid relaxation time, the start of 1D and 2D flexible cylinder oscillations were observed to occur at $\mathrm{Ma}_e = 0.2$ and 0.9, respectively. The elastic Mach number may be an appropriate dimensionless number to define the critical onset points of symmetric 1D and asymmetric 2D oscillations across different fluid properties and structural geometries for future studies. This number is a ratio of the flow velocity to the speed of an elastic wave propagating in the viscoelastic fluid. When the elastic Mach number is small, the governing equations are elliptic and the solutions are smooth. However, when the elastic Mach number becomes greater than one, the flow velocity becomes greater than the elastic wave speed, the governing equations change type from elliptic to hyperbolic, and elastic shock waves can propagate along fluid streamlines. In Ref. [60], the elastic Mach number was found to be much less than one; however, in Ref. [58] the flow instabilities were found to begin at an elastic Mach number of $\mathrm{Ma}_e = 1$ downstream of the cylinder, followed by upstream elastic instabilities at $\mathrm{Ma}_e \sim 10$. A similar flow pattern was also observed for a linear array of cylinders [59]. The results from these studies provide insight into understanding the transition of flexible cylinder oscillations from one to two dimensions. In this study, as with our previous study of flow past a flexible sheet [39], the elastic flow instability resulting in a 1D sawtooth oscillation pattern was found to occur for flows with an elastic Mach number less than 1. In fact, the flow past the flexible sheet never achieved an elastic Mach number greater than 1, which is perhaps why 2D oscillations were never observed. At higher flow velocities, the time-dependent asymmetricity of the flow field takes over as the dominant mechanism of flexible cylinder oscillations, just as it did in the cases of flow of a shear thinning polymer solutions past a rigid cylinder [57]. This transition was found to occur at an elastic Mach number close to 1, $\mathrm{Ma}_e = 0.9$. This suggests that the observed flow transition from 1D to 2D oscillations could be the result of a similar break in symmetry of the stagnation streamline observed by Riberio *et al.* [57] and that the eventual transition to highly asymmetric flow (Fig. 11) could be the result of a change in the underlying flow type from elliptic to hyperbolic as suggested by Shi *et al.* [58]. In Fig. 14, a vertical flow-induced birefringent strand can be seen as separating the region of fast-moving fluid from the slow-moving zone below the flexible cylinder during an asymmetric 2D oscillation. This strand may possibly represent an elastic wave

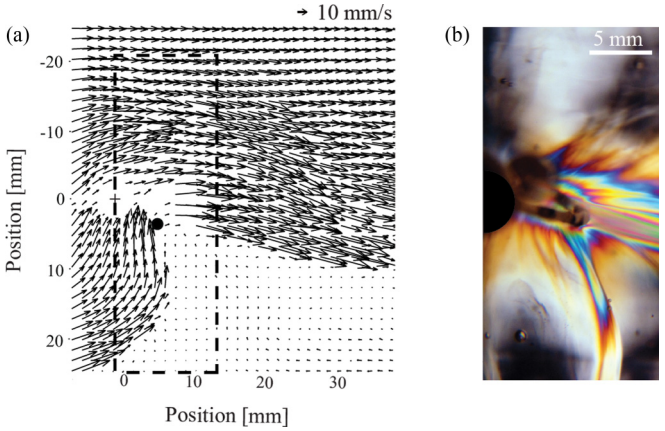

FIG. 14. (a) The PIV image of the flow around the flexible cylinder at $U = 11.5$ mm/s during an asymmetric 2D oscillation. (b) The dashed region of interest is presented through an FIB image. The flow is from left to right.

or the in-line compression and crossflow extensional deformation of the wormlike micelles which occur simultaneously as the flow is directed upward over the flexible cylinder as seen in the PIV image [Fig. 14(a)].

IV. CONCLUSION

In this paper, we have presented the results of our investigation of subjecting a flexible cylinder to a flow of viscoelastic wormlike micelle solution. The flow velocity was varied in order to study the onset of elastic flow instability accompanied by nonlinear oscillations of the flexible cylinder. Beyond a critical flow velocity, elastic flow instabilities occurring in the wake of the flexible cylinder were observed to induce two main types of oscillations, one and two dimensional, depending on the flow velocity tested. Beyond $U_{\text{crit}} = 2.7$ mm/s, the flexible cylinder oscillations were one dimensional in nature and in line with the flow direction with increasing amplitude and frequency. Velocity vector fields from PIV images and FIB images reveal the state of the flow field during these oscillations. At higher flow velocities, the breakdown of the wormlike micelle network was seen to occur locally at regions along the cylinder's span. As a result, the 1D oscillations were no longer in line with the flow direction. These observations relating to 1D flexible cylinder oscillations corroborate those reported in [39]. Beyond $U_{\text{crit}_{2D}} = 5.7$ mm/s, the asymmetry of the flow field progressed to become strong enough to force the flexible cylinder to rotate towards a sidewall and assume a new position where its oscillations become two dimensional in nature. Particle image velocimetry and FIB images have been used to study this dramatic transition of the flow field. During these 2D oscillations, the flexible cylinder was observed to be able to block off almost 50% of the incoming flow in spite of it providing only a blockage of 2.5% to the channel's cross section. The occurrence of 2D oscillations was seen to become more prevalent at higher flow velocities with increasing oscillation frequency but with decaying resultant amplitude.

Finally, by using a circular cylinder in these experiments, a direct comparison to the Newtonian FSI literature can be made for flow past a circular cylinder. For a circular cylinder placed in a flow of Newtonian fluid, the cylinder is stable and no oscillations are observed at $\text{Re} \sim 0$. Oscillations of the circular cylinder begin only at higher Reynolds number due to vortex shedding in the wake of the cylinder. However, the same is not true in viscoelastic fluids. Even at $\text{Re} \sim 0$, elastic fluid instabilities occur in the flow of viscoelastic fluids which drive the oscillations of a circular cylinder. In this paper, the flexible cylinder was observed to undergo periodic 1D and 2D oscillations at $\text{Re} = 10^{-4}$. Inertia plays no role in this structural response and vortex shedding is not the cause of the cylinder

oscillations. As described in Sec. I B, a long flexible circular cylinder in the flow of a Newtonian fluid traces a figure-eight orbit under lock-in conditions. The oscillations observed due to elastic fluid instabilities of a viscoelastic fluid, on the other hand, exhibit a sawtooth and elliptical pattern based on the type of cylinder oscillations. In general, lock-in was not observed during this study; however, the investigation of the possibility of finding a window of lock-in behavior for viscoelastic fluid-structure interactions is left for future study.

ACKNOWLEDGMENT

This work was funded by the National Science Foundation under Grant No. CBET-1705251.

[1] P. Flory, *Principles of Polymer Chemistry* (Cornell University Press, Ithaca, 1953).
[2] F. A. Morrison, *Understanding Rheology* (Oxford University Press, Oxford, 2001).
[3] V. J. Anderson, J. R. A. Pearson, and E. S. Boek, *Rheology Reviews* (British Society of Rheology, London, 2006), Vol. 4, pp. 217–253.
[4] S. Kefi, J. Lee, T. Pope, P. Sullivan, E. Nelson, A. Hernandez, T. Olsen, M. Parlar, B. Powers, A. Roy, A. Wilson, and A. Twynam, Expanding applications for viscoelastic surfactants, Oilfield Rev. **16**, 10 (2004).
[5] J. L. Zakin and H. W. Bewersdorff, Surfactant drag reduction, Rev. Chem. Eng. **14**, 253 (1998).
[6] J. P. Rothstein, *Rheology Reviews* (British Society of Rheology, London, 2008).
[7] L. M. Walker, Rheology and structure of worm-like micelles, Curr. Opin. Colloid Interface Sci. **6**, 451 (2001).
[8] J.-F. Berret, *Rheology of Wormlike Micelles: Equilibrium Properties and Shear Banding Transitions* (Springer Netherlands, Dordrecht, 2006), pp. 667–720.
[9] J. N. Israelachvili, *Intermolecular and Surface Forces: With Applications to Colloidal and Biological Systems* (Academic Press, London, 1985).
[10] R. G. Larson, *The Structure and Rheology of Complex Fluids* (Oxford University Press, New York, 1999).
[11] H. Rehage and H. Hoffmann, Viscoelastic surfactant solutions: Model systems for rheological research, Mol. Phys. **74**, 933 (1991).
[12] A. Bhardwaj, E. Miller, and J. P. Rothstein, Filament stretching and capillary breakup extensional rheometry measurements of viscoelastic wormlike micelle solutions, J. Rheol. **51**, 693 (2007).
[13] R. G. Laughlin, *The Aqueous Phase Behavior of Surfactants* (Academic, New York, 1994).
[14] J. Appell, G. Porte, A. Khatory, F. Kern, and S. J. Candau, Static and dynamic properties of a network of wormlike surfactant micelles (cetylpyridinium chlorate in sodium chlorate brine), J. Phys. II France **2**, 1045 (1992).
[15] J. P. Rothstein, Transient extensional rheology of wormlike micelle solutions, J. Rheol. **47**, 1227 (2003).
[16] S. Chen and J. P. Rothstein, Flow of a wormlike micelle solution past a falling sphere, J. Non-Newtonian Fluid Mech. **116**, 205 (2004).
[17] G. R. Moss and J. P. Rothstein, Flow of wormlike micelle solutions through a periodic array of cylinders, J. Non-Newtonian Fluid Mech. **165**, 1 (2010).
[18] G. R. Moss and J. P. Rothstein, Flow of wormlike micelle solutions past a confined circular cylinder, J. Non-Newtonian Fluid Mech. **165**, 1505 (2010).
[19] J. R. Gladden and A. Belmonte, Motion of a Viscoelastic Micellar Fluid around a Cylinder: Flow and Fracture, Phys. Rev. Lett. **98**, 224501 (2007).
[20] H. Mohammadigoushki and S. J. Muller, Sedimentation of a sphere in wormlike micellar fluids, J. Rheol. **60**, 587 (2016).
[21] P. W. Bearman, Vortex shedding from oscillating bluff bodies, Annu. Rev. Fluid Mech. **16**, 195 (1984).
[22] T. Sarpkaya, A critical review of the intrinsic nature of vortex-induced vibrations, J. Fluid. Struct. **19**, 389 (2004).

[23] C. H. K. Williamson and R. Govardhan, Vortex-induced vibrations, Annu. Rev. Fluid Mech. **36**, 413 (2004).
[24] P. W. Bearman, Circular cylinder wakes and vortex-induced vibrations, J. Fluid. Struct. **27**, 648 (2011).
[25] A. Ongoren and D. Rockwell, Flow structure from an oscillating cylinder Part 1. Mechanisms of phase shift and recovery in the near wake, J. Fluid Mech. **191**, 197 (1988).
[26] J. Carberry, J. Sheridan, and D. Rockwell, Controlled oscillations of a cylinder: Forces and wake modes, J. Fluid Mech. **538**, 31 (2005).
[27] J. S. Leontini, B. E. Stewart, M. C. Thompson, and K. Hourigan, Wake state and energy transitions of an oscillating cylinder at low Reynolds number, Phys. Fluids **18**, 067101 (2006).
[28] T. K. Prasanth and S. Mittal, Vortex-induced vibrations of a circular cylinder at low Reynolds numbers, J. Fluid Mech. **594**, 463 (2008).
[29] D. Jeon and M. Gharib, On circular cylinders undergoing two-degree-of-freedom forced motions, J. Fluid. Struct. **15**, 533 (2001).
[30] N. Jauvtis and C. H. K. Williamson, The effect of two degrees of freedom on vortex-induced vibration at low mass and damping, J. Fluid Mech. **509**, 23 (2004).
[31] J. M. Dahl, F. S. Hover, M. S. Triantafyllou, S. Dong, and G. E. Karniadakis, Resonant Vibrations of Bluff Bodies Cause Multivortex Shedding and High Frequency Forces, Phys. Rev. Lett. **99**, 144503 (2007).
[32] J. M. Dahl, F. S. Hover, M. S. Triantafyllou, and O. H. Oakley, Dual resonance in vortex-induced vibrations at subcritical and supercritical Reynolds numbers, J. Fluid Mech. **643**, 395 (2010).
[33] A. D. Trim, H. Braaten, H. Lie, and M. A. Tognarelli, Experimental investigation of vortex-induced vibration of long marine risers, J. Fluid. Struct. **21**, 335 (2005).
[34] B. Seyed-Aghazadeh and Y. Modarres-Sadeghi, Reconstructing the vortex-induced-vibration response of flexible cylinders using limited localized measurement points, J. Fluid. Struct. **65**, 433 (2016).
[35] J. K. Vandiver, V. Jaiswal, and V. Jhingran, Insights on vortex-induced, traveling waves on long risers, J. Fluid. Struct. **25**, 641 (2009).
[36] Y. Modarres-Sadeghi, H. Mukundan, J. M. Dahl, F. S. Hover, and M. S. Triantafyllou, The effect of higher harmonic forces on fatigue life of marine risers, J. Sound Vib. **329**, 43 (2010).
[37] R. Bourguet, G. E. Karniadakis, and M. S. Triantafyllou, Distributed lock-in drives broadband vortex-induced vibrations of a long flexible cylinder in shear flow, J. Fluid Mech. **717**, 361 (2013).
[38] G. H. McKinley, P. Pakdel, and A. Oztekin, Rheological and geometric scaling of purely elastic flow instabilities, J. Non-Newtonian Fluid Mech. **67**, 19 (1996).
[39] A. A. Dey, Y. Modarres-Sadeghi, and J. P. Rothstein, Experimental observation of viscoelastic fluid-structure interactions, J. Fluid Mech. **813**, 5 (2017).
[40] R. B. Bird, R. C. Armstrong, and O. Hassager, *Dynamics of Polymeric Liquids: Volume 1 Fluid Mechanics* (Wiley, New York, 1987).
[41] P. Fischer and H. Rehage, Rheological master curves of viscoelastic surfactant solutions by varying the solvent viscosity and temperature, Langmuir **13**, 7012 (1997).
[42] M. E. Cates, Reptation of living polymers: Dynamics of entangled polymers in the presence of reversible chain-scission reactions, Macromolecules **20**, 2289 (1987).
[43] R. Granek and M. E. Cates, Stress relaxation in living polymers: Results from a Poisson renewal model, J. Chem. Phys. **96**, 4758 (1992).
[44] M. Doi and S. F. Edwards, *The Theory of Polymer Dynamics* (Oxford University Press, Oxford, 1986).
[45] A. Bhardwaj, D. Richter, M. Chellamuthu, and J. P. Rothstein, The effect of preshear on the extensional rheology of wormlike micelle solutions, Rheol. Acta **46**, 861 (2007).
[46] J. Drappier, D. Bonn, J. Meunier, S. Lerouge, J.-P. Decruppe, and F. Bertrand, Correlation between birefringent bands and shear bands in surfactant solutions, J. Stat. Mech. (2006) P04003.
[47] G. G. Fuller, *Optical Rheometry of Complex Fluids* (Oxford University Press, New York, 1995).
[48] T. Shikata, S. J. Dahman, and D. S. Pearson, Rheo-optic behavior of wormlike micelles, Langmuir **10**, 3470 (1994).
[49] E. K. Wheeler, P. Fischer, and G. G. Fuller, Time-periodic flow induced structures and instabilities in a viscoelastic surfactant solution, J. Non-Newtonian Fluid Mech. **75**, 193 (1998).
[50] R. Cressely and R. Hocquart, Localized flow birefringence induced in the wake of obstackles, Opt. Acta **27**, 699 (1980).

[51] C. Chen and G. G. Warr, Light scattering from wormlike micelles in an elongational flow, Langmuir **13**, 1374 (1997).
[52] F. P. T. Baaijens, S. H. A. Selen, H. P. W. Baaijens, G. W. M. Peters, and H. E. H. Meijer, Viscoelastic flow past a confined cylinder of a low density polyethylene melt, J. Non-Newtonian Fluid Mech. **68**, 173 (1997).
[53] M. D. Chilcott and J. M. Rallison, Creeping flow of dilute polymer-solutions past cylinders and spheres, J. Non-Newtonian Fluid Mech. **29**, 381 (1988).
[54] A. Afonso, M. A. Alves, F. T. Pinho, and P. J. Oliveira, Uniform flow of viscoelastic fluids past a confined falling cylinder, Rheol. Acta **47**, 325 (2008).
[55] E. Miller and J. P. Rothstein, Transient evolution of shear-banding wormlike micellar solutions, J. Non-Newtonian Fluid Mech. **143**, 22 (2007).
[56] T. Divoux, M. A. Fardin, S. Manneville, and S. Lerouge, Shear banding of complex fluids, Annu. Rev. Fluid Mech. **48**, 81 (2016).
[57] V. M. Ribeiro, P. M. Coelho, F. T. Pinho, and M. A. Alves, Viscoelastic fluid flow past a confined cylinder: Three-dimensional effects and stability, Chem. Eng. Sci. **111**, 364 (2014).
[58] X. Shi, S. Kenney, G. Chapagain, and G. F. Christopher, Mechanisms of onset for moderate mach number instabilities of viscoelastic flows around confined cylinders, Rheol. Acta **54**, 805 (2015).
[59] X. Shi and G. F. Christopher, Growth of viscoelastic instabilities around linear cylinder arrays, Phys. Fluids **28**, 124102 (2016).
[60] G. H. McKinley, R. C. Armstrong, and R. A. Brown, The wake instability in viscoelastic flow past confined circular cylinders, Philos. Trans. R. Soc. A **344**, 265 (1993).
[61] H. H. Hu and D. D. Joseph, Numerical simulation of viscoelastic flow past a cylinder, J. Non-Newtonian Fluid Mech. **37**, 347 (1990).